Synaptic memristor based on two-dimensional layered WSe_2 nanosheets with short- and long-term plasticity

Songwen Luo,[a] Kanghong Liao,[a] Peixian Lei,[a] Ting Jiang,[a] Siyi Chen,[a] Qin Xie,[b] Wenbo Luo,[b] Wen Huang,[b] Shuoguo Yuan,[c] Wenjing Jie,*[a] and Jianhua Hao,*[c]

Neural synapses with diverse synaptic functions of short- and long-term plasticity are highly desired for developing complex neuromorphic system. Memristor with its two terminals respectively serving as pre- and post-neurons can emulate two neuronal-based synaptic functions. In this work, multilayer two-dimensional (2D) layered WSe_2 nanosheets are synthesized by a salt-assisted chemical vapor deposition (CVD) method. Two-terminal memristors with planar structure are fabricated based on the CVD-grown triangular WSe_2 nanosheets. The fabricated devices exhibit typical bipolar nonvolatile resistive switching behaviors with high current ON/OFF ratio up to 6×10^3 and good retention and endurance properties, suggesting good stability and reliability of WSe_2-based memristor. Furthermore, the developed memristors demonstrate synaptic functions of short- and long-term plasticity (STP and LTP) as well as the transition between STP to LTP by applying consecutive pulse voltages. Moreover, the WSe_2-based memristor exhibits biological synaptic functions of long-term potentiation and depression, and paired-pulse facilitation. Thus, our 2D WSe_2 nanosheet based memristors not only exhibit stable and reliable nonvolatile resistive switching behaviors, but also show potential applications in mimicking biological synapses.

Introduction

Recently, artificial synapses have been extensively investigated to emulate biological synaptic functionality and mimick neuromorphic system in human brain. Neural synapses with diverse synaptic functionality of short- and long-term plasticity are highly desired for developing complex neuromorphic system for applications in artificial neural networks.[1,2] Many electronic devices, such as two-terminal memristors, three-terminal field effect transistors (FETs), have been demonstrated to emulate synaptic functionality.[3,4] Among them, memristors with controllable resistive switching (RS) behaviors are widely studied as promising candidates for neural synaptic devices. A memristor is a two-terminal device with its resistance changing dependent on the applied voltages. With the development of two-dimensional (2D) materials, memristors based on such 2D layered nanosheets are extensively studied owing to their low-power consumption and high-performance multifunctionality.[5] Besides, 2D materials provide a feasible way to construct memristors with atomic-precision scale and further fabricate RS devices based on various van der Waals (vdW) heterostructures. A large number of 2D materials have been employed in the memristors, ranging from semimetal of graphene,[6] semiconductor of transition metal dichalcogenides (TMDCs),[7] to insulator of hexagonal boron.[8] Among them, MoS_2 as a representative of TMDCs is the most widely studied 2D material in RS devices. From the first example of gate-tunable memristor reported in 2015 to the first demonstration of multiterminal memtransistor in 2018,[9,10] RS devices based on MoS_2, have drawn much attention from scientific research to technological applications. Similar to its counterpart MoS_2, WSe_2 possesses a layer-number dependent band gap and its indirect band gap in bulk changes into direct band gap in its monolayer.[11] On the other hand, multilayer WSe_2 shows ambipolar transport properties, which is different MoS_2 with n-type behaviors due to the unavoidable presence of S vacancies.[12] Moreover, owing to the ambipolar properties and low doping levels, 2D layered WSe_2 has strong spin/valley coupling and demonstrates promising possibility of alternative to new valleytronic and spintronic materials.[13] This opens up the opportunity to generate new and interesting RS behaviors and relevant physical mechanism by fabricating memristors based on the unique 2D layered WSe_2 materials. However, research focusing on memristor based on 2D layered WSe_2 is still limited.[14,15] It is highly desirable to build WSe_2 based memristors with reliable memristive properties and diverse synaptic functions which are suitable for applications in neural networks. Moreover, several published works about RS behaviors based on WSe_2 focus on the memristor with vertical structure.[16,17] In this work, memristors with planar structure were fabricated based on the triangle WSe_2 nanosheets synthesized by a salt-assisted chemical vapor deposition (CVD) method. Compared to previously reported memristors based on 2D WSe_2 nanosheets, our devices showed good stability and reliability with the ON/OFF ratio nearly 10^3 during longer retention time and for much more switching cycles. The constructed memristors also demonstrated synaptic functions of short- and long-term plasticity, suggesting potential

applications in biological synapses and complex neural networks.

Experimental

Material Synthesis

2D layered WSe_2 nanosheets were prepared on SiO_2 substrates by a salt-assisted CVD method using precursors of selenium (Se) and tungsten trioxide (WO_3) powders. In our experiments, the salt of potassium chloride (KCl) was introduced and mixed with WO_3 powder in order to reduce the melting point of WO_3 and accelerate the overall reaction rate.[18,19] In the CVD process, 100 mg WO_3 powder mixed with a small amount of KCl was placed in an alumina boat and put about 30 cm downstream of the boat of 190 mg Se powder. The target substrates were placed on the boat downstream of the mixed powder of KCl and WO_3, as schematically shown in Fig. S1. The two boats were heated independently to 300 and 1000 ℃ for the Se and WO_3 powder, respectively. Then, after the reaction, both boats naturally cooled to room temperature. The tube furnace was gassed with a 60 standard cubic centimetres per minute (sccm) flow of mixed gases of 95% argon (Ar) and 5% hydrogen (H_2) during all the heating, growth and cooling processes.

Device Fabrication

In our experiments, the SiO_2 layer in the oxidized Si substrate could be damaged due to the high growth temperature of WSe_2 nanosheets. By considering the subsequent electrical measurements, the CVD-grown multilayer nanosheets were transferred onto SiO_2/Si substrate through standard transferring method by using polymethyl methacrylate (PMMA). Then, the two terminal memristors were fabricated by depositing Ag electrodes through photolithography on the individual WSe_2 nanosheet. To be more specific, Ag electrodes were prepared by using sputtering method. The photoresist and excess Ag were removed by ultrasonic method with acetone. Then, the fabricated devices were dried at 100 ℃ for 1 min. Finally, Ag electrodes with the thickness of ~ 100 nm and distance of 4 μm between each other were fabricated on individual WSe_2 nanosheet to form two-terminal memristor.

Characterizations and Measurements

Field emission scanning electron microscope (FE-SEM JSM-7500, JEOL, Japan) was used to characterize the surface morphology of the fabricated WSe_2 nanosheets. Atomic force microscope (AFM DI Nanoscope 8) was employed to determine the thickness of the nanosheets. Furthermore, Raman spectra and PL measurements were performed by confocal Raman system (HORIBA LabRAM HR Evolution) with the excitation laser wavelength of 532 nm. Besides, X-ray photoelectron spectroscopy (XPS Thermo Scientific ESCALAB 250Xi) was used to investigate the elemental composition of the prepared nanosheets. All electrical properties were characterized by using the double-channel source meter (Keithley 2636B) with a four-probe station system. All electrical measurements were performed at room temperature.

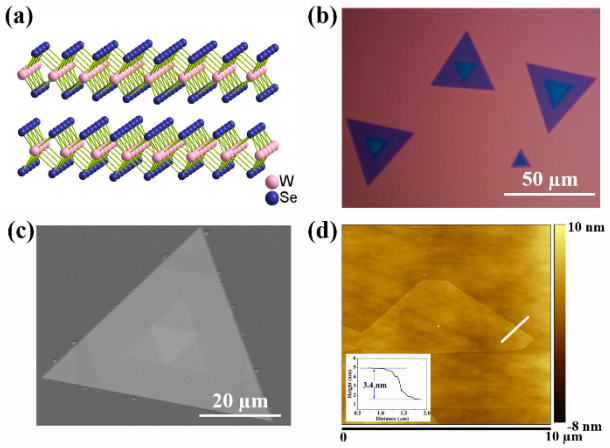

Fig. 1 Characterization of the CVD-grown WSe_2 nanosheets. (a) Schematic of the crystal structure of WSe_2. (b) Optical image of triangular WSe_2 nanosheets grown on 285 nm SiO_2/Si substrate. (c) SEM image of one typical triangular WSe_2 flake. (d) AFM image of a small WSe_2 flake. Inset shows the height profile corresponding to the white line in the AFM image.

Results and discussion

Fig. 1a shows the schematic of structure for bilayer WSe_2. A single-layer WSe_2 is composed of one layer of W atom sandwiched by two layers of Se atoms with thickness of ~ 0.75 nm.[20] In our experiments, triangular WSe_2 nanosheets were synthesized by a salt-assisted CVD method. Fig. 1b shows the typical optical image of the triangular nanosheets with the size of several to dozens of micrometres. Especially, for the samples with the size over dozens of micrometres, small triangular nanosheets were grown on the top surface of the underlying large triangles, suggesting the multilayer nature of the prepared nanosheets. The small triangular nanosheets possess the same or 180 ° angle spacing compared with the underlying samples. The surface morphology of the synthesized triangular nanosheets is characterized by FE-SEM, as shown in Fig. 1c. The SEM image shows a typical sample with three triangles in the sequence of a big one on the bottom, a small one possessing the same angle spacing with the underlying big one in the middle, and then one smaller possessing 180 ° angle spacing on the top. The energy dispersive EDX is used to analyse the elements on the surface. The element mapping analysis shows that W and Se elements are evenly distributed in the WSe_2 nanosheet, as shown in Fig. S2. The stoichiometry of W and Se is measured to be 1:2.08, suggesting the well prepared WSe_2 nanosheets and the existence of W vacancies in the samples.[21,22] In addition, AFM is used to characterize the surface morphology and determine the thickness of the prepared WSe_2 nanosheet, as shown in Fig. 1d. The flake possesses smooth surface with the thickness of about 3.4 nm, suggesting the layer number of 5.

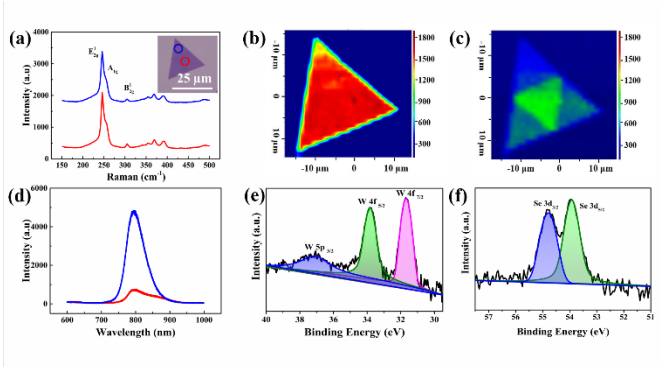

Fig. 2. Characterization of the multilayer triangular WSe_2 nanosheets. (a) Raman spectra characterized from the two spots marked in the inset, respectively. Inset: optical image of a typical WSe_2 flake. (b) Raman mapping at 246 cm^{-1} (E_{2g}^1 mode). (c) Raman mapping at 305 cm^{-1} (B_{2g}^1 mode). (d). PL spectra characterized from the two spots, respectively, marked in the inset of a. (e) XPS spectrum of W 4f and W 5p. (f) XPS spectrum of Se 3d.

Next, confocal Raman spectroscopy was used to characterize the CVD-grown triangular WSe_2 nanosheets. Two typical Raman spectra (red and blue) are observed from two spots located at the centre and surrounding of the triangle, respectively, as shown in Fig. 2a and the inset of the optical image for the triangle nanosheet. Two feature peaks are located at 246 cm^{-1} and 255 cm^{-1}, corresponding to in-plane of E_{2g}^1 and out-of-plane mode of A_{1g}, respectively.[20,23] For atomic-thin WSe_2 samples, the A_{1g} mode is shown as the shoulder peak of E_{2g}^1 mode. The feature peak located at 305 cm^{-1} is B_{2g}^1 mode which originates from the interlayer coupling effect, suggesting the multilayer nature of the CVD-grown nanoflake²⁴²⁴.[24] Besides, the intensity of B_{2g}^1 mode in the centre (red line) of the triangle is higher than that of the surrounding triangle (blue line), indicating the centre triangle is thicker than the surrounding one. Furthermore, Raman intensity mapping is performed using feature peaks E_{2g}^1 and B_{2g}^1 to characterize the uniformity of the CVD-grown sample. Fig. 2b shows the Raman mapping image of E_{2g}^1 mode at 246 cm^{-1}. A clear triangle consistent with the sample shown in the optical image (inset of Fig. 2a) can be observed in the Raman mapping image. The measured signal from E_{2g}^1 mode is intense and uniform throughout the overall triangle, suggesting the WSe_2 nanosheet is well synthesized by the salt-assisted CVD method. Fig. 2c shows the Raman mapping image of interlayer B_{2g}^1 mode at 305 cm^{-1}. A relatively light triangle surrounded by a dark triangle can be observed in the Raman mapping image, consistent with the optical image (inset of Fig. 2a) with a small triangle on the top surface of the bottom triangular sample. Thus, through the salt-assisted CVD method, we can synthesize multilayer WSe_2 nanosheet. Moreover, photoluminescence (PL) measurements have been performed, as shown in Fig. 2d. The red and blue spectra are observed from the red and blue spots marked in the inset of Fig. 2a, respectively. The blue spectrum shows an intense PL peak located at 795 nm, corresponding to the band gap of 1.56 eV. For the red one, the PL intensity dramatically decreases, and a shoulder peak at low energy can be observed, suggesting the transition from direct to indirect band gap when atomically thin layers evolving from thin to thick thickness. Besides, the CVD-grown samples are studied by XPS, as shown in Fig. 2e and f. The W element valence spectrum is fitted to double peaks of $W4f_{5/2}$ at 33.8 eV and $W4f_{7/2}$ at 31.7 eV and a single peak of $W5p_{3/2}$ at 37.5 eV. As shown in Fig. 2f, the Se element valence spectrum can be well fitted into two peaks, $Se3d_{3/2}$ at 54.8 eV and $Se3d_{5/2}$ at 53.95 eV, which is consistent with previously reported works.[25,26]

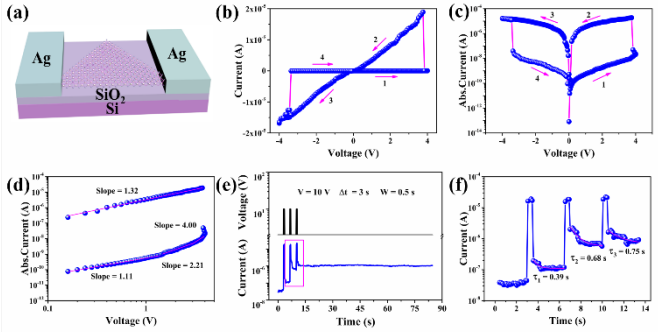

Fig. 3. RS performance of WSe_2-based memristor. (a) Schematic of the RS device based on the multilayer WSe_2 nanosheet. (b) Typical *I–V* curve plotted using double-linear coordinates. (c) The *I–V* curve re-plotted with current using logarithmic coordinate. (d) The positive part of the *I–V* curve re-plotted using double-logarithmic coordinates and linear fitting of the curve. (e) The current responses of input three voltage pulses with amplitude of 10 V and after removing the input pulses. (f) Fitting three current decay curves marked in e.

The lateral memristor based on multilayer WSe_2 nanosheet was fabricated by using Ag as electrodes on SiO_2/Si substrate, as schematically shown in Fig. 3a. The detailed device fabrication process and RS measurement information can refer to our previous reports.[27–30] Initially, no obvious RS behaviours can be observed, as shown in Fig. S3. The initial sweeping cycles corresponds to the forming process for our fabricated devices. After several cycles, the typical bipolar non-volatile RS behaviours can be detected, as shown in Fig. 3b. Fig. 3c shows the current–voltage (*I–V*) curve with the current in logarithmic scale. For forward scanning, the current suddenly increased at ~ 4 V, corresponding to the "SET" process from a high resistance state (HRS) to a low resistance state (LRS). For backward scanning, the LRS can be maintained, then turned to HRS at ~ – 3.5 V, suggesting the "RESET" process. The *I–V* curve confirms that the CVD-grown multilayer WSe_2 nanosheet processes the non-volatile bipolar RS behaviours with the ON/OFF current ratio of ~ 6×10^3 at the read voltage of 0.5 V. Moreover, 10 experimental switching loops of the *I–V* curves are shown in Fig. S4 to examine the cycle-to-cycle variation. The WSe_2-based memristor exhibits repeatable RS cycles without remarkable changes in the SET and RESET voltages and ON/OFF ratios, suggesting good stability of the fabricated device. In our experiments, 36 memristors were fabricated by using the CVD-grown triangular WSe_2 nanosheets to test the device-to-device variation. The statistical analysis of the RS parameters, including ON/OFF ratio, set and reset voltages, of the prepared memristors are shown in Fig. S5. Although there are some device-to-device fluctuations, all the 36 memristors possess bipolar non-volatile RS behaviors and the RS performance of the 36 memristors are comparable. The

majority of the memristors possess bipolar non-volatile RS behaviours with the ON/OFF current ratio of 10^3 and SET/REST voltage of ± 4 V, suggesting the reliability of such CVD-grown WSe_2 nanosheets for fabrication of memristors.

To further understand the RS behaviours of the memristor, the positive part of Fig. 3c is re-plotted using double-logarithmic coordinates, as shown in Fig. 3d. In the LRS, the *I*–*V* curve shows nearly linear behaviours, suggesting Ohmic contact between the Ag electrode and the WSe_2 nanosheet. In the HRS, the curve can be divided into three portions according to $I \sim V^a$, including an Ohmic region (a ≈ 1), a Child's law region (a ≈ 2) and a followed region where a > 2. This is the typical space charge limited current (SCLC) injection for the RS behaviours. In our experiments, we measured the temperature dependent resistance of the memristor at the LRS (Fig. S6). At the LRS, the device shows the semiconducting conductive behaviors rather than the metallic conductance. Thus, we can rule out the possibility of forming Ag filaments. Moreover, the WSe_2 layers demonstrate *p*-type transport properties, as shown in Fig. S7 (See Electronic Supplementary Information). This result is also consistent with previous studies of *p*-type behaviours of multilayer WSe_2.[25,31] Besides, XPS results show that the atomic ratio of W to Se is 1: 2.08, indicating that there are W vacancies in our synthesized WSe_2 layers. For the fabricated devices, the device is at the HRS initially. When a bias voltage larger than the SET voltage is applied, the W vacancies can contribute to the formation of the conductive filaments, giving rise to the LRS. Herein, we can conclude that our observed bipolar RS behaviours are resulted from the WSe_2 nanosheets rather than the Ag electrodes.

Moreover, the fresh device without forming also can be triggered by applying three pulse voltages with an amplitude of 10 V, pulse width (W) of 0.5 s and pulse time interval (Δ*t*) of 3 s. The amplitude of the pulse voltages is larger than the SET voltage of the device. Initially, the current dramatically decreases after the first stimulation, suggesting volatile RS behaviours, as shown in Fig. 3e. However, the current still shows a slight increase compared to the initial HRS through a gradual decay. A continuous increase also can be observed after the second stimulation, suggesting the existence of historical effect of previous- on post-stimulation. When the pulse voltages are removed after three pulses, the historical effect of previous stimulation can be retained. The device can stay at the LRS without any decay for a long period after removing the consecutive input pulses, suggesting the non-volatile behaviours. In addition, the current decay curves can be well fitted using the exponential function of $I = I_0 + I_A \exp(t / \tau)$, where I_0 stands for the current offset, I_A is the fit constant, *t* is the time after each input pulse, and τ is the relaxation time constant which can be used to evaluate the forgetting rate in the decay curves. As shown in Fig. 3f, the value of τ gradually increases from 0.39 to 0.75 s as the number of pulses increases. The continuously increasing value of τ confirms the existence of historical effect of previous spikes on post-stimulation.

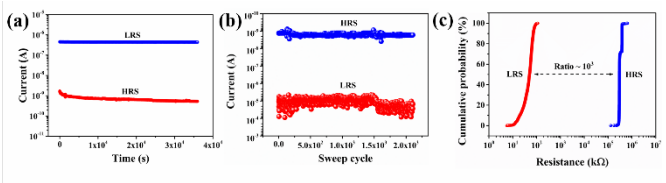

Fig. 4. (a) Retention characteristics of the memristor. (b) Endurance performance of the memristor. (c) Cumulative probability of LRS and HRS.

The retention and endurance properties of WSe_2-based memristor were measured at room temperature. Fig. 4a illustrates the retention characteristics with read voltage of 0.5 V. Both the HRS and LRS remain almost unchanged during the entire period of measurement. The memristor shows good stability and undetectable degradation with the ON/OFF ratio up to 8.4×10^2 during the retention time up to 3.6×10^4 s, suggesting the non-volatile behaviours of the WSe_2-based memristors. Moreover, the retention lifetime was further estimated. The ON/OFF ratio even after 10 years can still be expected to be nearly 10^3 according to the power-law extrapolation (See Fig. S8 in the Electronic Supplementary Information). Fig. 4b shows the endurance characteristics of the memory device under pulse conditions. The resistances of both HRS and LRS are measured by applying pulses with the W = 1 s, Δ*t* = 9 s and magnitude of 10 V for SET and – 10 V for RESET, respectively. The memristor is highly reliable and maintains the high ON/OFF ratio up to 1.6×10^3 for 2100 cycles without noticeable degradation, conforming the excellent endurance. Based on statistical analysis of endurance curves, the cumulative probability of LRS and HRS is plotted and shown in Fig. 4c. The reliable switching behaviours can be clearly observed, suggesting distinguishable HRS and LRS with ON/OFF ratio up to 10^3. Therefore, our devices show good stability and reliability with the ON/OFF ratio nearly 10^3 during longer retention time and for much more switching cycles compared to previously reported memristors based on 2D WSe_2 nanosheets.[16,17,32–35]

Furthermore, our WSe_2-based two-terminal memristor can emulate two neuronal-based biological synapses, as schematically shown in Fig. 5a. The synaptic plasticity, i.e., the ability to control and retain the synaptic weight over time, can be classified into two forms: short-term plasticity (STP) and long-term plasticity (LTP). The synaptic weight can be estimated by the postsynaptic current (PSC) induced by sequential voltage pulses as the presynaptic input.[36,37] Fig. 5b shows the time-dependent PSC by applying consecutive input spikes with an amplitude of 3 V, W = 0.5 s and Δ*t* = 3 s. It should be noted that the amplitude of the pulse voltages is smaller than the SET voltage (~ 4 V) of the memristor. Initially, the increased PSC under the stimulations of the applied pulses can recover to its original value, suggesting the typical STP characteristics. After a series of pulse voltages, the historical effect of previous stimulation on post-stimulation can be observed. A transition from STP to LTP can be achieved by increasing the number of the input spikes.[38] Moreover, the PSC decay curves also can be fitted using the exponential function. The relaxation time constant τ can be used calulated to

evaluate the forgetting rate in the LTP decay curves. As shown in Fig. 5c, the value of τ gradually increases from 0.16 to 1.21 s as the number of pulses increases. The continuously increasing value of τ proves the existence of historical effect of previous spikes on post-stimulation. Then, the amplitude of the pulse voltages is increased to 6 V, larger than the SET voltage of the memristor, as shown in Fig. 5d. In this case, the historical effect of previous pulse voltages is enhanced. The PSC gradually increases as the consecutive input spikes are stimulated at the synapse, showing the LTP characteristics. The LTP behaviours can be initially observed, suggesting the increased amplitude of the pulse voltages can improve the synaptic weight.[39] Herein, for a small input spikes with the amplitude smaller than the SET voltage, the device initially shows typical STP characteristics, and then a transition from STP to LTP due to the historical effect of previous pulse voltages. For a large input spikes with the amplitude larger than the SET voltage, the device shows LTP characteristics. The synaptic functions of STP and LTP suggest potential applications of our 2D WSe_2 nanosheet based memristor in artificial neural networks.

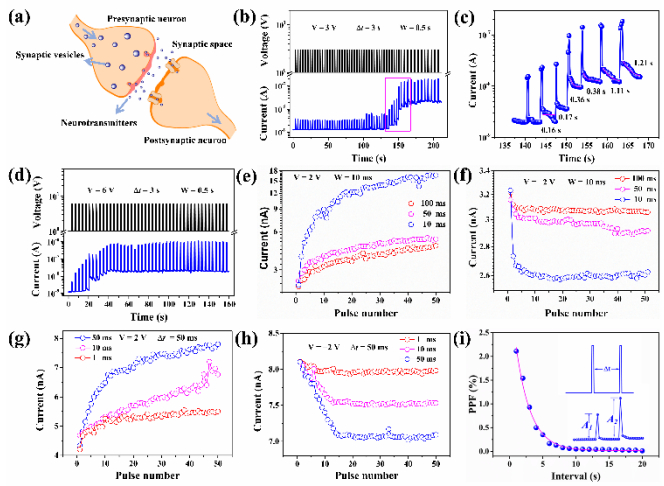

Fig. 5. Synaptic functions of multilayer WSe_2-based memristor (a) Schematics of two neuronal-based synaptic functions. (b) PSC responses with short-term plasticity characteristics under input spikes with amplitude of 3 V. (c) Fitting current decay curves marked in b. (d) PSC responses with long-term plasticity characteristics under input spikes with amplitude of 6 V. (e) Long-term potentiation behaviours under voltage pulses with different pulse intervals ranging from 10 to 100 ms. (f) Long-term depression behaviours under voltage pulses with different pulse intervals ranging from 10 to 100 ms. (g) Long-term potentiation with different pulse width ranging from 1 to 50 ms. (h) Long-term depression with different pulse width ranging from 1 to 50 ms. (i) PPF as a function of the time interval between two sequential pulses.

Similar to biological synapses, the synaptic plasticity of our WSe_2-based memristor can be modulated not only by the amplitude of the pulse voltages, but also by the time interval, Δ*t*. The long-term potentiation behaviours are shown when sequential voltage pulses are introduced to the pre-synapse, as shown in Fig. 5e. All the pulse sequences with the amplitude of 2 V and the pulse interval ranging from 10 to 100 ms can induce exponential potentiation in the PSC. Notably, a shorter pulse interval can generate a relatively fast potentiation process. Moreover, Fig. 5f shows the long-term depression induced by negative pulse sequences. Similarly, a shorter pulse also can lead to a relatively slow depression process. The memristors demonstrate long-term potentiation and depression under positive and negative pulse sequences, respectively, suggesting the potential applications of our memristor in emulation of the excitation and inhibition for biological synapses. In addition to the current response to pulse voltages with different pulse intervals, we also measured the long-term potentiation and depression functions with different pulse width, as shown in Figs. 5g&h. The more linear conductance change can be achieved in the long-term depression (Fig. 5h) of the current response of the pulse sequence pulses with amplitude of − 2 V, interval of 50 ms and width ranging from 1 to 50 ms. Furthermore, the paired-pulse facilitation (PPF) is a physiological phenomenon which is an enhancement effect of a previous stimulation on a subsequent response.[40,41] The synaptic plasticity can be estimated by the PPF feature when the synapse is stimulated by two sequential pulse voltages. As shown in the inset of Fig. 5i, the PPF index can be defined as the expression $(A_2 - A_1) / A_1 \times 100$ %, where A_1 and A_2 are the current response of the synapse stimulated by the first and the second pulse voltages, respectively. Fig. 5f shows the PPF index as a function of the Δ*t*. The PPF index exponentially decays as the Δ*t* increases with the decaying time constant of 2.2 s. The exponential decay is consistent with the behaviours of biological synapses. Herein, the WSe_2-based memristor exhibits comprehensive biological synaptic functions and plasticity, including the STP, LTP, long-term potentiation and depression, and paired-pulse facilitation, which can efficiently emulate the biological synapses.

Conclusions

In summary, planar memristors were fabricated based on the CVD-grown triangular WSe_2 nanosheets with Ag as electrodes. The fabricated device exhibited typical bipolar nonvolatile RS behaviors with high current ON/OFF ratio of 6×10^3 and good retention and endurance properties, suggesting excellent reproducibility and reliability of WSe_2-based memristor. Furthermore, the memristor demonstrated synaptic functionality of STP and LTP as well as the transition between them. For a small input spikes with the amplitude smaller than the SET voltage, the device initially showed typical STP characteristics, and then a transition from STP to LTP due to the historical effect of previous pulse voltages. For the input spikes with large amplitude, the device demonstrated LTP characteristic. Moreover, the WSe_2-based memristor exhibited biological synaptic functions of long-term potentiation and depression, and paired-pulse facilitation, suggesting potential applications in mimicking biological synapses.

Conflicts of interest

There are no conflicts to declare.

Acknowledgements

This work was supported by the grants from National Natural Science Foundation of China (61974097), the Open Foundation of State Key Laboratory of Electronic Thin Films and Integrated Devices (KFJJ201805), Sichuan Youth Science and Technology Foundation (2019JDJQ0052) and Hong Kong RGC GRF (PolyU 153033/17P).

References

1 S. Ambrogio, P. Narayanan, H. Tsai, R. M. Shelby, I. Boybat, C. Di Nolfo, S. Sidler, M. Giordano, M. Bodini, N. C. P. Farinha, B. Killeen, C. Cheng, Y. Jaoudi and G. W. Burr, *Nature*, 2018, **558**, 60–67.

2 W. Zhang, B. Gao, J. Tang, P. Yao, S. Yu, M. F. Chang, H. J. Yoo, H. Qian and H. Wu, *Nat. Electron.*, 2020, **3**, 371–382.

3 D. Li, B. Wu, X. Zhu, J. Wang, B. Ryu, W. D. Lu, W. Lu and X. Liang, *ACS Nano*, 2018, **12**, 9240–9252.

4 C. Sen Yang, D. S. Shang, N. Liu, G. Shi, X. Shen, R. C. Yu, Y. Q. Li and Y. Sun, *Adv. Mater.*, 2017, **29**, 1700906.

5 T. Y. Wang, J. L. Meng, Z. Y. He, L. Chen, H. Zhu, Q. Q. Sun, S. J. Ding, P. Zhou and D. W. Zhang, *Adv. Sci.*, 2020, **7**, 1903480.

6 M. T. Sharbati, Y. Du, J. Torres, N. D. Ardolino, M. Yun and F. Xiong, *Adv. Mater.*, 2018, **30**, 1802353.

7 R. Ge, X. Wu, M. Kim, J. Shi, S. Sonde, L. Tao, Y. Zhang, J. C. Lee and D. Akinwande, *Nano Lett.*, 2018, **18**, 434–441.

8 X. Wu, R. Ge, P. A. Chen, H. Chou, Z. Zhang, Y. Zhang, S. Banerjee, M. H. Chiang, J. C. Lee and D. Akinwande, *Adv. Mater.*, 2019, **31**, 1–7.

9 V. K. Sangwan, D. Jariwala, I. S. Kim, K. S. Chen, T. J. Marks, L. J. Lauhon and M. C. Hersam, *Nat. Nanotechnol.*, 2015, **10**, 403–406.

10 V. K. Sangwan, H. S. Lee, H. Bergeron, I. Balla, M. E. Beck, K. S. Chen and M. C. Hersam, *Nature*, 2018, **554**, 500–504.

11 Q. Cheng, J. Pang, D. Sun, J. Wang, S. Zhang, F. Liu, Y. Chen, R. Yang, N. Liang, X. Lu, Y. Ji, J. Wang, C. Zhang, Y. Sang, H. Liu and W. Zhou, *InfoMat*, 2020, **2**, 656–697.

12 A. Allain and A. Kis, *ACS Nano*, 2014, **8**, 7180–7185.

13 M. Tahir, *Phys. E Low-Dimensional Syst. Nanostructures*, 2018, **97**, 184–190.

14 D. Xiang, T. Liu, J. Xu, J. Y. Tan, Z. Hu, B. Lei, Y. Zheng, J. Wu, A. H. C. Neto, L. Liu and W. Chen, *Nat. Commun.*, 2018, **9**, 2966.

15 S. Seo, S. H. Jo, S. Kim, J. Shim, S. Oh, J. H. Kim, K. Heo, J. W. Choi, C. Choi, S. Oh, D. Kuzum, H. S. P. Wong and J. H. Park, *Nat. Commun.*, 2018, **9**, 5106.

16 M. Sivan, Y. Li, H. Veluri, Y. Zhao, B. Tang, X. Wang, E. Zamburg, J. F. Leong, J. X. Niu, U. Chand and A. V. Y. Thean, *Nat. Commun.*, 2019, **10**, 5201.

17 R. Ge, X. Wu, M. Kim, J. Shi, S. Sonde, L. Tao, Y. Zhang, J. C. Lee and D. Akinwande, *Nano Lett.*, 2018, **18**, 434–441.

18 J. Zhou, J. Lin, X. Huang, Y. Zhou, Y. Chen, J. Xia, H. Wang, Y. Xie, H. Yu, J. Lei, D. Wu, F. Liu, Q. Fu, Q. Zeng, C. H. Hsu, C. Yang, L. Lu, T. Yu, Z. Shen, H. Lin, B. I. Yakobson, Q. Liu, K. Suenaga, G. Liu and Z. Liu, *Nature*, 2018, **556**, 355–359.

19 P. Yang, Z. Zhang, M. Sun, F. Lin, T. Cheng, J. Shi, C. Xie, Y. Shi, S. Jiang, Y. Huan, P. Liu, F. Ding, C. Xiong, D. Xie and Y. Zhang, *ACS Nano*, 2019, **13**, 3649–3658.

20 E. Corro, H. Terrones, A. Elias, C. Fantini, S. Feng, M. A. Nguyen, T. E. Mallouk, M. Terrones, M. A. Pimenta, D. De Fisica, U. Federal, D. M. Gerais, A. A. Carlos, C. Postal, B. Horizonte, D. E. L. Corro and E. T. Al, *ACS Nano*, 2014, **8**, 9629–9635.

21 D. Yang, X. Fan, F. Zhang, Y. Hu and Z. Luo, *Nanoscale Res. Lett.*, 2019, **14**, 192.

22 S. Zhang, C. G. Wang, M. Y. Li, D. Huang, L. J. Li, W. Ji and S. Wu, *Phys. Rev. Lett.*, 2017, **119**, 046101.

23 J.-K. Huang, J. Pu, C.-L. Hsu, M.-H. Chiu, Z.-Y. Juang, Y.-H. Chang, W.-H. Chang, Y. Iwasa, T. Takenobu and L. Lain-Jong, *ACS Nano*, 2013, **8**, 923–930.

24 H. Zhou, C. Wang, J. C. Shaw, R. Cheng, Y. Chen, X. Huang, Y. Liu, N. O. Weiss, Z. Lin, Y. Huang and X. Duan, *Nano Lett.*, 2015, **15**, 709–713.

25 C. H. Chu, H. C. Lin, C. H. Yeh, Z. Y. Liang, M. Y. Chou and P. W. Chiu, *ACS Nano*, 2019, **13**, 8146–8154.

26 C. Perumalveeramalai, F. Li, T. Guo and T. W. Kim, *IEEE Electron Device Lett.*, 2019, **40**, 1088–1091.

27 Y. Yang, H. Du, Q. Xue, X. Wei, Z. Yang, C. Xu, D. Lin, W. Jie and J. Hao, *Nano Energy*, 2019, **57**, 566–573.

28 H. Du, J. Chen, M. Tu, S. Luo, S. Li, S. Yuan, T. Gong, W. Huang, W. Jie and J. Hao, *J. Mater. Chem. C*, 2019, **7**, 12160–12169.

29 M. Tu, H. Lu, S. Luo, H. Peng, S. Li, Y. Ke, S. Yuan, W. Huang, W. Jie and J. Hao, *ACS Appl. Mater. Interfaces*, 2020, **12**, 24133–24140.

30 H. Du, M. Tu, S. Luo, Y. Liu, X. Qiu, H. Lu, S. Li, S. Yuan, W. Huang, W. Jie and J. Hao, *Appl. Phys. Lett.*, 2020, **116**, 253102.

31 L. Kong, X. Zhang, Q. Tao, M. Zhang, W. Dang, Z. Li, L. Feng, L. Liao, X. Duan and Y. Liu, *Nat. Commun.*, 2020, **11**, 1866.

32 R. Ge, X. Wu, L. Liang, S. M. Hus, Y. Gu, E. Okogbue, H. Chou, J. Shi, Y. Zhang, S. K. Banerjee, Y. Jung, J. C. Lee and D. Akinwande, *Adv. Mater.*, 2020, 2007792.

33 H. K. He, R. Yang, H. M. Huang, F. F. Yang, Y. Z. Wu, J. Shaibo and X. Guo, *Nanoscale*, 2020, **12**, 380–387.

34 H. K. He, F. F. Yang and R. Yang, *Phys. Chem. Chem. Phys.*, 2020, **22**, 20658–20664.

35 Y. Li, X. Feng, M. Sivan, J. F. Leong, B. Tang, X. Wang, J. N. Tey, J. Wei, K. W. Ang and A. V. Y. Thean, *IEEE Sens. J.*, 2020, **20**, 4653–4659.

36 T. Chang, S. H. Jo and W. Lu, *ACS Nano*, 2011, **5**, 7669–7676.

37 T. Ohno, T. Hasegawa, T. Tsuruoka, K. Terabe, J. K. Gimzewski and M. Aono, *Nat. Mater.*, 2011, **10**, 591–595.

38 Y. Shi, X. Liang, B. Yuan, V. Chen, H. Li, F. Hui, Z. Yu, F. Yuan, E. Pop, H. S. P. Wong and M. Lanza, *Nat. Electron.*, 2018, **1**, 458–465.

39 X. F. Lin Wang, Wugang Liao, Swee Liang Wong, Zhi Gen Yu, Sifan Li, Yee-Fun Lim, C. Z. Wee Chong Tan, Xin Huang, Li Chen, Liang Liu, Jingsheng Chen, Xiao Gong and and K.-W. A. Xinke Liu, Yong-Wei Zhang,* Dongzhi Chi, *Adv. Funct. Mater.*, 2019, **19**, 2411–2417.

40 M. Kumar, D. K. Ban, S. M. Kim, J. Kim and C. P. Wong, *Adv. Electron. Mater.*, 2019, **5**, 1900467.
41 X. Yan, C. Qin, C. Lu, J. Zhao, R. Zhao, D. Ren, Z. Zhou, H. Wang, J. Wang, L. Zhang, X. Li, Y. Pei, G. Wang, Q. Zhao, K. Wang, Z. Xiao and H. Li, *Adv. Mater.*, 2019, **29**, 1606927.